

submitted to *International Journal of Computer Vision* June, 2002

The Dual-Bootstrap Iterative Closest Point Algorithm with Application to Retinal Image Registration

Charles V. Stewart¹

Chia-Ling Tsai¹

Badrinath Roysam²

¹Dept. of Computer Science
Rensselaer Polytechnic Institute
Troy, New York 12180–3590
stewart,tsaic@cs.rpi.edu

²Dept. of Electrical, Computer,
and
Systems Engineering
Rensselaer Polytechnic Institute
Troy, New York 12180–3590
roysab@rpi.edu

June 24, 2002

Abstract

A new generalization of the Iterative Closest Point (ICP) registration algorithm is introduced and incorporated into a complete algorithm for registering retinal images. ICP works by iterating two steps: matching points based on the current transformation estimate and refining the estimate based on the matches. It requires a good initial estimate. By contrast, the Dual-Bootstrap ICP algorithm only requires an initial estimate that is a “toe hold” on the correct alignment — accurate only locally, over a small image region, and perhaps using a lower-order transformation than is needed to accurately align the entire images. The algorithm iteratively “bootstraps” both the region over which the model is accurate and the chosen transformation model, using a robust version of standard ICP restricted to the bootstrap region during each iteration. The covariance of the transformation estimate controls both bootstrap processes. The algorithm is designed to handle several difficult circumstances in registration: (a) data from which relatively poor initial estimates can be reliably obtained, (b) data that has structural (geometric) complexity such as multiple proximate curves and surfaces, (c) data that has many missing or extraneous points, and (d) image pairs that have low overlap. In registering retinal image pairs, the Dual-Bootstrap ICP algorithm is initialized from similarity transformation estimates obtained by matching individual or pairs of vascular landmarks, and it aligns images based on blood vessel centerlines to produce quadratic transformations. On tests involving approximately 6000 image pairs, it successfully registered 99.5% of the pairs containing at least one common landmark, and 100% of the pairs containing at least one common landmark and 35% overlap or higher. This near flawless performance enables a variety of applications.

Index terms: Registration, iterative closest point, robust estimation, retinal imaging

1 Introduction

1.1 The Iterative Closest Point Algorithm

The iterative closest point (ICP) registration algorithm was invented almost simultaneously in the early 1990's by several different research groups [3, 12, 14, 49, 78], and has been used in many different applications since then [22, 43, 49, 55]. ICP is a point-based registration algorithm, where the "points" may be raw measurements such as (x, y, z) values from range images, intensity points in three-dimensional medical images [24, 29], and edge elements, corners and interest points [64] that locally summarize the geometric structure of the data. ICP should be used when correspondences between the point sets are not known and when matching based on the properties of individual points (and their surroundings) does not produce a large enough set of unique correspondences to precisely align the two data sets.

To fix the idea of the ICP algorithm, let I_1 and I_2 denote the two data sets and let θ be the parameter vector of the transformation mapping the coordinate system of I_1 onto the coordinate system of I_2 . ICP iterates two main steps: (1) using a fixed estimate, $\hat{\theta}$, the transformation is applied to each point from image dataset I_1 and the closest point in image dataset I_2 is found as a temporary match, and (2) using constraints formed from these matches, a new best estimate $\hat{\theta}$ is computed. (In some cases, matches are only formed implicitly [12].) This process is repeated until the estimate $\hat{\theta}$ stabilizes. Different instantiations of the ICP algorithm use different combinations of image points, distance metrics, and transformation models. These affect convergence rates and accuracy, but not the general structure of the algorithm. Clearly, as an iterative minimization algorithm, ICP requires proper initialization, and a variety of techniques may be used: application specific constraints [54, 55], image-wide measures on the data sets such as statistical moments and geometric attributes [35, 38], multiresolution methods [24], and initial matching of distinctive features [16, 19, 67, 74].

The literature on ICP has concentrated on initialization, efficient matching [1, 60], and applications, while leaving the algorithmic structure unchanged. The motivating observation of this paper is different, however: there are situations where initial estimates alone are not enough to ensure that ICP will converge to an accurate transformation estimate. We illustrate the problem in the context of registering images of the human retina and then consider general properties of the problem. Figure 1 shows two different images of the same retina taken at the same

time. The viewpoint of the images is somewhat different, and different regions of the retina are well-focused in the images. The features used in registration are the branching and cross-over points of the vasculature (seen in Figure 1(a) and (b)) and the centerline points of the vasculature (Figure 1(c) and (d)). The former are used for initialization of ICP, whereas the latter are used in the iterative steps of ICP. In this case, only the landmark circled in (a) and (b) is in common between the two images. Computing an initial similarity transformation based on aligning this landmark and the surrounding vasculature yields the alignment shown in Figure 2(a). Starting a robust version of ICP algorithm from this initial estimate and letting it converge yields the incorrect result shown in Figure 2(b). This is based on using a similarity transformation throughout and then switching at the end to a quadratic transformation [11] that accounts for the curvature of the retina. If instead the quadratic transformation is used immediately, a similar incorrect result is obtained.

This example illustrates a general problem with ICP algorithms — convergence to an incorrect final registration starting from an initial estimate that locally appears correct. Since ICP algorithms have been used successfully in a variety of applications, it is important to outline the circumstances under which this problem can arise. An intuitive discussion is given here, with a technical analysis saved for later in the paper. The problem can arise under a combination of the following four circumstances:¹

Geometric data complexity: Repetitive structures such as meshes, multiple elongated structures such as blood vessels and nerve fibers, and high-frequency structure such as in brain images create many opportunities for mismatches when there are even small misalignments. Such complexity raises the level of accuracy required in the initial estimate.

Data quality: Low data quality means that points and even whole structures (e.g. individual blood vessels) can appear in one image, but be missing in another. (For the images in Figure 1, within the region that is common between the images only 63% of the centerline points are in common; image-wide this drops to 58%.) These “outliers” can cause mismatches that skew the parameter estimates, converting small misalignments into much larger ones.

¹We are ignoring for this paper the difficulties of multimodal registration where different imaging modalities make completely different structures — bone vs. soft tissue — prominent [22].

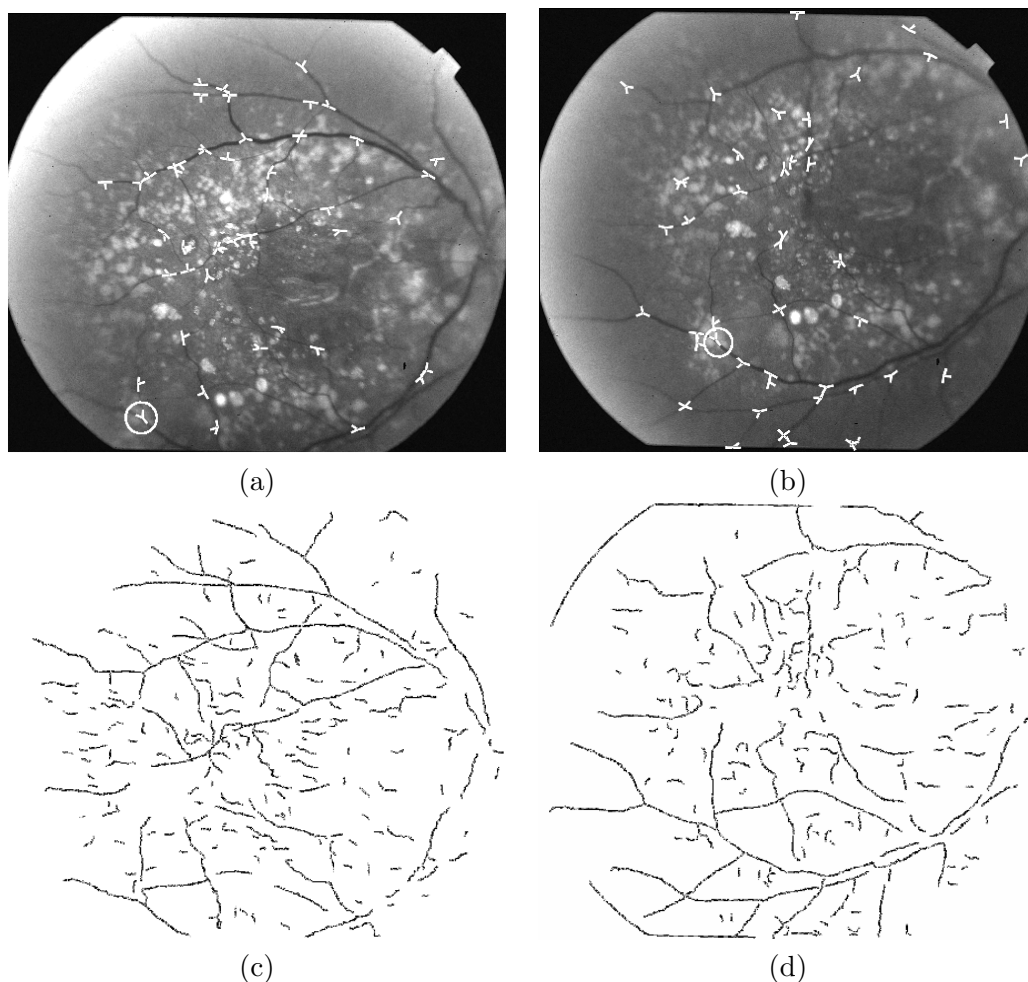


Figure 1: Illustrating retinal fundus images of an unhealthy eye (nonexudative age-related macular degeneration) together with image features used in ICP registration. Panels (a) and (b) show the images, with landmarks extracted by our retinal image tracing algorithm [8, 27]. The landmarks are branching and cross-over points of the retinal vasculature. These are used in initializing ICP. Panels (c) and (d) show the centerline points obtained by the tracing algorithm and used in the iterative steps of ICP. Many inconsistencies in the two sets of traces may be observed.

Low overlap: Low overlap can cause similar problems to low-quality data, except that there is coherence to what's missing — entire image regions. Low overlap is challenging for initialization based on image-wide measures and on multiresolution methods. Moreover, it raises the level of significance of each constraint used in registration, implying that more accuracy is required of each.

High-order transformation models: These require more constraints to initialize and can introduce greater distortions in the data sets. In the example shown, a 12-parameter,

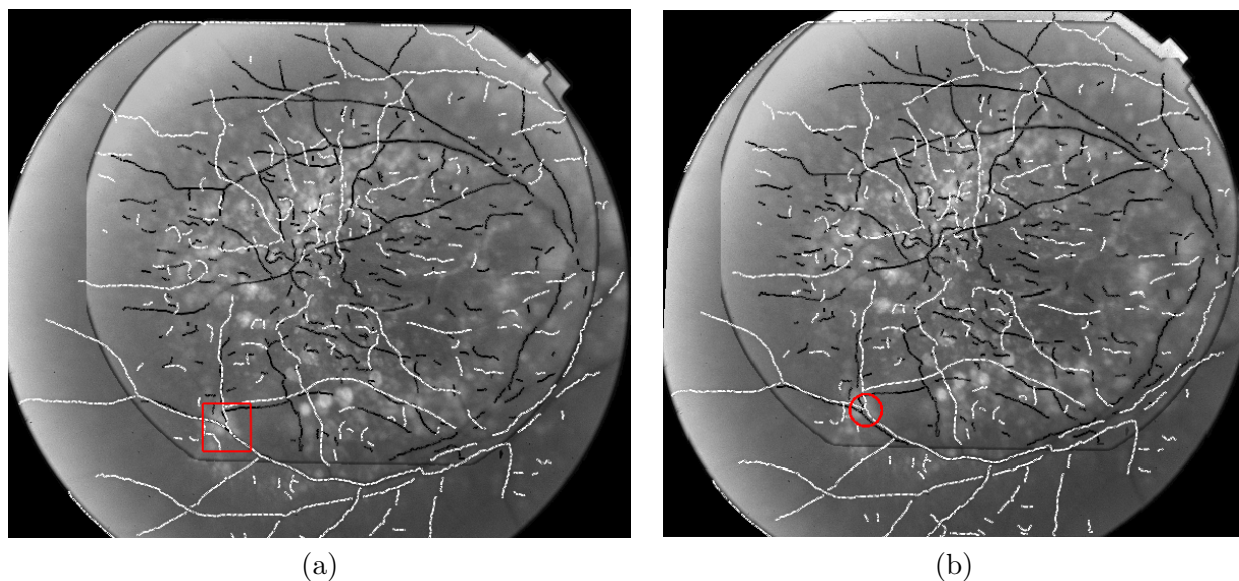


Figure 2: The results of applying standard ICP to the images shown in Figure 1. Panel (a) shows the initial alignment based on the single correct correspondence. Trace points from the image shown in Figure 1(a) are shown in black and trace points from the image shown in Figure 1(b) are shown in white. The red square on the bottom left shows the accurate alignment surrounding the initial correspondence. Panel (b) shows the alignment result after ICP convergence. The alignment is extremely poor due to the mismatches in the upper region.

quadratic transformation is necessary to solve the registration problem, but it can't be estimated accurately from the single correct initial landmark correspondence.

1.2 The Dual-Bootstrap ICP Algorithm: Main Ideas

This paper presents a new registration algorithm, called the “Dual Bootstrap ICP”, that is designed to handle each of these circumstances. It works when initialization provides just a “toehold” on the correct estimate of the transformation, and successfully registers images such as the pair shown in Figure 1. The approach, demonstrated in Figure 3, is based on three important ideas:

The Bootstrap Region: The algorithm works on the “bootstrap region”. This region, R , is defined as the image region over which the transformation is considered accurate. It determines a set of points to which the ICP algorithm is applied. Initially, R is small, surrounding the points used to generate an initial estimate. The bootstrap region is gradually grown (bootstrapped) to an image-wide, accurate transformation estimate.

Robust ICP: A robust version of ICP, including a carefully estimated error scale, is used

throughout the bootstrapping process to avoid skewed estimates due to mismatches.

Bootstrapping the Model: Rather than using a single, fixed transformation model, different models are used in different bootstrap regions, starting from a simple model for the initial bootstrap region and gradually evolving to a higher-order model as the bootstrap region grows to describe the entire data set. Model selection techniques [7, 75], which depend fundamentally on the parameter estimate covariance matrix, are used to automatically select the transformation model for each bootstrap region.

Thus, the term “dual-bootstrap” refers to simultaneous growth in the bootstrap region and the transformation model order. It is applied to one or more initial bootstrap regions independently, ending with success when one bootstrap region R is expanded to a sufficiently-accurate, image-wide transformation.

1.3 Retinal Image Registration

The Dual-Bootstrap ICP algorithm is described as a general technique, but then applied to retinal image registration. This is an important application and, as shown above, illustrates the major difficulties of ICP registration. Registering retinal images taken at different times — with time gaps ranging from minutes, to hours, to days, to a year or more — can form the basis for measuring (a) the effect of surgery [25, 40, 61, 69], (b) the progress of diseases [34, 41, 42, 48], and (c) the impact of drugs and nutritional supplements [20, 28, 52]. Retinal image registration can also be used for montaging images to obtain a complete view of the retina, and to integrate ordinary retinal fundus images with angiograms showing blood flow in both the retinal and choroidal vasculature [18, 73].

2 Robust ICP Problem Formulation

We start by presenting a mathematical problem formulation for point-based registration algorithms. This will provide a formal context for the main contributions of the Dual-Bootstrap ICP algorithm. One difference between this formulation and standard versions is the use of robust estimation [31, 59, 70].

The formulation starts with two sets of point vectors, $\mathcal{P} = \{\mathbf{p}_i\}$ from image I_1 and $\mathcal{Q} = \{\mathbf{q}_j\}$

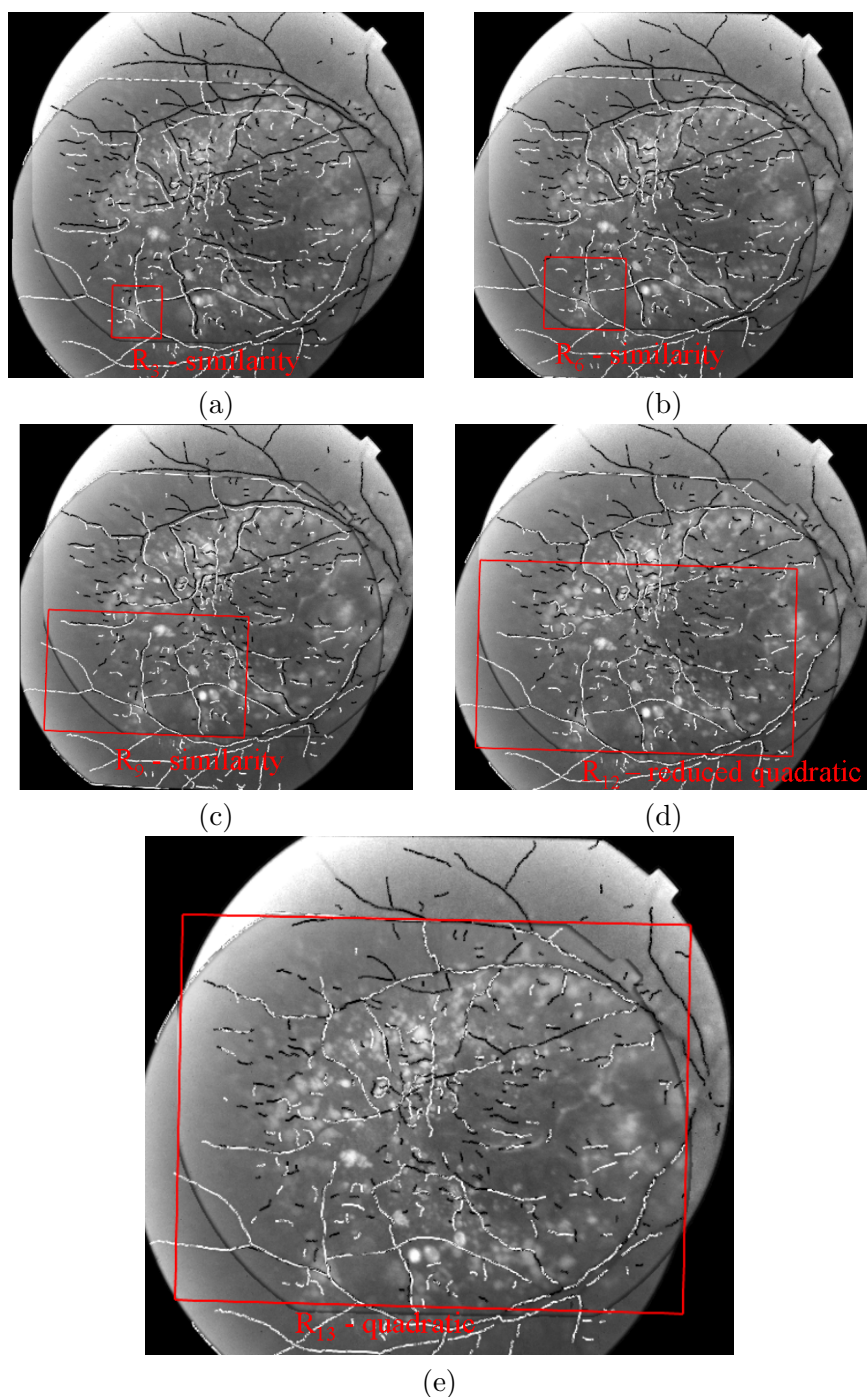


Figure 3: Illustrating the Dual Bootstrap ICP algorithm in retinal image registration using the images and feature points shown in Figure 1 and the initial alignment shown in Figure 2. In each iteration, a robust version of ICP is applied *only* in the bootstrap region, R_t , indicated by the red rectangle in each figure. The transformation is only required to be accurate in this bootstrap region. Also in each iteration, the best transformation model (in this case, similarity, reduced-quadratic, or quadratic — see Table 1) is automatically selected *and* the bootstrap region is grown. Several increments of this process are shown in the panels, and the model selected in each bootstrapping iteration is indicated. Panel (e) shows the final alignment using a 12-parameter quadratic model.

from image I_2 . These points could be as simple as $(x, y, z)^T$ coordinates taken from range images, or they could be descriptions of edge elements, interest points [64, 68], corner locations [32], or other image structures. The problem is to find the transformation parameters, $\boldsymbol{\theta}$, and associated set of correspondences, $\mathcal{C} \subset \mathcal{P} \times \mathcal{Q}$, that minimize an appropriate error distance. A general objective function to be minimized can be written as

$$E(\boldsymbol{\theta}, \sigma; \mathcal{C}) = \sum_{(\mathbf{p}_i, \mathbf{q}_j) \in \mathcal{C}} \rho(d(M(\boldsymbol{\theta}; \mathbf{p}_i), \mathbf{q}_j)/\sigma). \quad (1)$$

The components of this objective function are described as follows:

- $M(\boldsymbol{\theta}; \mathbf{p}_i)$ is the mapping of \mathbf{p}_i into the coordinate system of I_2 based on transformation parameter vector $\boldsymbol{\theta}$. A common and simple case of this mapping is a rigid transformation of a point coordinate vector from \mathfrak{R}^n to \mathfrak{R}^n . The mapping may be more general and it may be extended to apply to tangent vectors, normal vectors, and other geometric or even photometric properties [23, 39].
- $d(M(\boldsymbol{\theta}; \mathbf{p}_i), \mathbf{q}_j)$ is a distance metric in the coordinate system of I_2 between the mapped vector and the corresponding vector \mathbf{q}_j .² The distance metric depends on the types of point vectors. For detected corner points, interest points or other image landmarks, the natural metric is the Euclidean distance. For points that are samples from smooth regions of curves or surfaces, point-to-line or point-to-plane normal distances are generally more appropriate [3, 14]. These alternatives are illustrated using an example in Figure 4. Algebraically, if $\hat{\boldsymbol{\eta}}_j$ is the line (2d) or plane (3d) normal, then the normal distance is

$$d(M(\boldsymbol{\theta}; \mathbf{p}_i), \mathbf{q}_j) = |(M(\boldsymbol{\theta}; \mathbf{p}_i) - \mathbf{q}_j)^T \hat{\boldsymbol{\eta}}_j|.$$

Combinations of constraints are also possible.

- $\rho(u)$ is a robust loss function [31, 59, 70], monotonically non-decreasing as a function of $|u|$. A least-squares loss function is obtained by making $\rho(u) = u^2$, but because mismatches are common, robust loss functions, which down-grade the significance of mismatches, are crucial [31, 59, 70]. See Figure 5 for plots of example functions.

²See [33, Ch. 3] for formulations where error distances are measured in both images. These more complicated minimization problems are beyond the scope of our discussion.

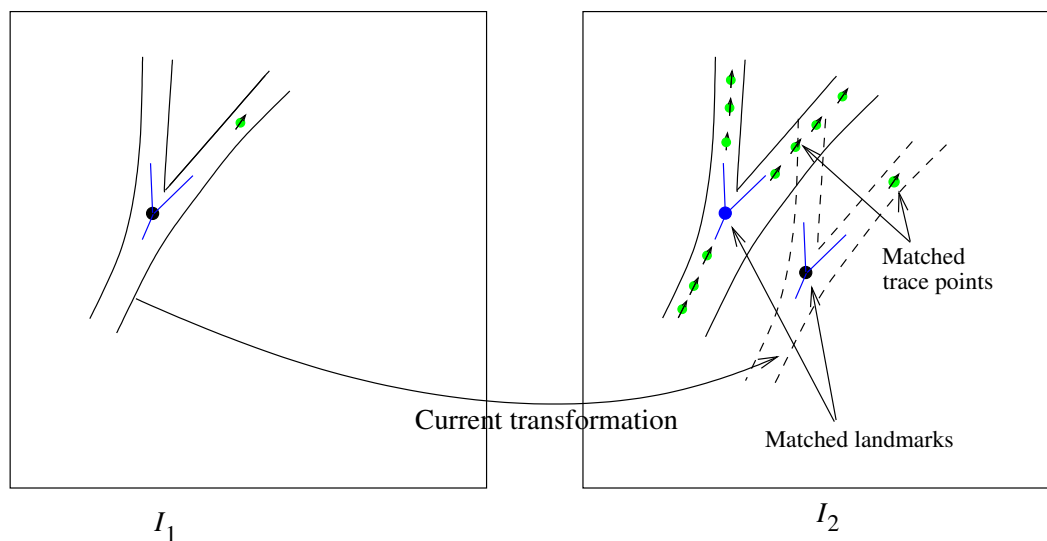


Figure 4: A schematic illustrating distance metrics on landmarks and on trace centerpoints. The region around a vascular landmark is shown in I_1 , including the landmark location itself and a separate trace point. These are mapped onto I_2 using the current transformation and matched against the landmark location and trace points. The landmark location match should generate a Euclidean distance constraint, whereas the trace point match, which is in fact mismatched slightly, should generate constraint that measures point-to-line distance. The line is the local, linear approximation to the contour, with tangent vectors shown.

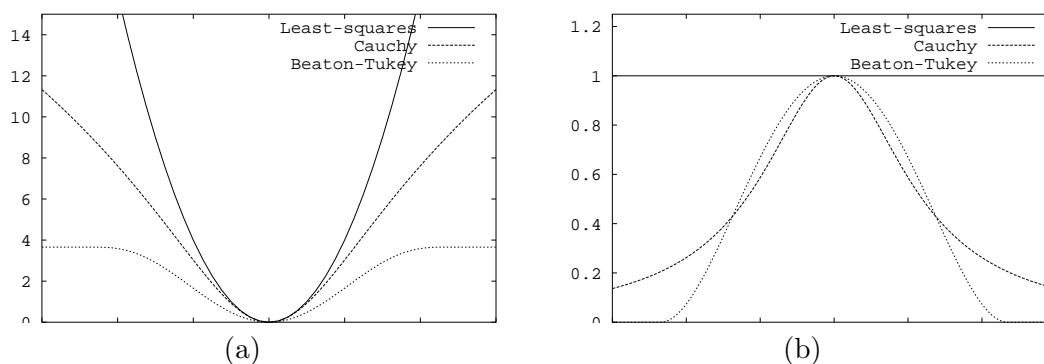


Figure 5: Plots of the robust loss function $\rho(u)$ (a) and weight function $w(u) = \rho'(u)/u$ (b) for the Beaton-Tukey biweight loss function, the Cauchy loss function and the quadratic loss function, which equates to least-squares estimation. The weight function is used in the iteratively reweighted least-squares implementation of M-estimators [36]. The Beaton-Tukey is chosen because it most aggressively rejects outliers, providing no weight to matches with normalized distances greater than about 4 standard deviations.

- σ is the error scale, which is the (robust) standard deviation of the error distances. This must be estimated carefully: when the estimate $\hat{\sigma}$ is too small correct correspondences may be treated as outliers, but when $\hat{\sigma}$ is too large mismatches may be treated as inliers. Either case causes bias in the transformation estimate. A different issue is that as written, the

objective function shown in (1) is minimized by $\sigma \rightarrow \infty$. This can be avoided by adding a $\log(\sigma)$ term [37] or by (robustly) estimating and then fixing σ using a separate process during minimization [70].

- To avoid the trivial minimum corresponding to $\mathcal{C} = \{\}$, restrictions are often placed on \mathcal{C} . A common one is to make \mathcal{P} a subset of the points from I_1 and require a single correspondence in \mathcal{C} for each $\mathbf{p} \in \mathcal{P}$. We will make this assumption throughout the paper.

Various instantiations of the ICP algorithm differ primarily in the type of data, and the choices of mapping function and distance metric. They also differ in the data representations and matching techniques, but mainly these are implementation details. Once these are specified and the data sets and initial value of $\boldsymbol{\theta}$ are provided, ICP is straightforward. It simply works by alternately fixing $\boldsymbol{\theta}$ and estimating \mathcal{C} and then fixing \mathcal{C} and estimating $\boldsymbol{\theta}$, repeating until convergence. Multiple starting points may be provided and the ICP algorithm may be embedded in a multiresolution hierarchy, but our primary concern is the algorithm itself. Once substantial improvements are made, the new algorithm can be combined with a variety of initialization techniques. The improvements made will allow convergence to a desirable estimate from weaker initial conditions, reducing the significance of initialization.

3 The Dual-Bootstrap ICP Algorithm

The improvements of the Dual-Bootstrap ICP algorithm are obtained through manipulating the structure of the objective function (1) during minimization. The final minimization is the same however. This manipulation is done in two ways:

- The image I_1 point set \mathcal{P} is not treated as fixed. Instead, it is dictated by the bootstrap region, R , which starts as a small, compact subset of the image I_1 data and eventually grows to encompass the entire portion of I_1 that overlaps I_2 . We denote the sequence of regions by (R_1, \dots, R_t, \dots) where the subscript t indicates the iteration number, and write the point set as $\mathcal{P}_t = \mathcal{P}(R_t)$ to indicate the region dependency.
- A set of transformation models M and associated parameter vectors $\boldsymbol{\theta}$ is used, not just a single model. We denote the model set by $\{M_1, \dots, M_f\}$ and the sets of associated parameter vectors by $\{\boldsymbol{\theta}_1, \dots, \boldsymbol{\theta}_f\}$. One of these models is automatically selected for each

bootstrap region, R_t . The set of models may or may not form a nested hierarchy. The model set is needed when the data from which the estimates are initialized does not provide enough information for a reliable estimate of the parameters of the full model. (A restricted form of the Dual-Bootstrap ICP algorithm can be used with only a single model.) Let M_{m_t} denote the model selected at iteration t for region R_t , and let $\hat{\theta}_{m_t}$ denotes the associated estimate of the model parameter vector.

Thus, at each iteration of the Dual-Bootstrap ICP algorithm, a 6-tuple is determined:

$$(R_t, \mathcal{P}_t, \mathcal{C}_t, M_{m_t}, \hat{\theta}_{m_t}, \hat{\sigma}_t).$$

As the algorithm converges, R_t should stabilize on the portion of I_1 overlapping I_2 , \mathcal{C}_t should be a correct set of correspondences for this region, M_{m_t} should be the full model, and $\hat{\theta}_{m_t}$ and $\hat{\sigma}_t$ should approach the correct model and scale parameters.

3.1 Algorithm Outline

The outline of the actual algorithm is straightforward given the above discussion. It is again important to note that the Dual-Bootstrap ICP algorithm is an iterative minimization technique and therefore procedures outside the algorithm should provide the starting estimate. Thus, the following description is based on a single starting estimate.

1. Establish the initial bootstrap region R_1 in a small area around where the initial estimate is computed, and initialize model M_{m_1} to be the lowest order model.
2. $t = 1$;
3. While the estimate has not converged
 - (a) Select the points \mathcal{P}_t from R_t .
 - (b) Apply robust ICP to determine the correspondence set, \mathcal{C}_t , the transformation estimate $\hat{\theta}_{m_t}$, and the scale estimate $\hat{\sigma}_t$. Calculate the covariance matrix, Σ_{m_t} , of the estimate.
 - (c) Bootstrap the model: using the correspondence set, \mathcal{C}_t , and the covariance matrix Σ_{m_t} , apply a model selection technique to choose the new model $M_{m_{t+1}}$. If $M_{m_t} \neq M_{m_{t+1}}$,

calculate a new covariance matrix.

- (d) Bootstrap the region: Use the covariance matrix, Σ_{m_t} , and the new model $M_{m_{t+1}}$ to expand the region based on the covariance propagation error. The growth rate is inversely related to the error.
- (e) Check for convergence. The algorithm will converge just like normal ICP after the bootstrap region, R_t , stabilizes.
- (f) $t = t + 1$

Details are described in the following subsections.

3.2 Bootstrap Regions

For simplicity, the bootstrap regions R_t are rectangular. Other region shapes may be used without affecting the structure of the algorithm.

3.3 Covariance and Transfer Error

The covariance matrix of the parameter vector estimate [71] is needed in both model selection and region growth. The parameter estimate is denoted by $\hat{\theta}$. The covariance matrix is approximated by the inverse Hessian of $E(\hat{\theta})$

$$\Sigma_{m_t} = \mathbf{H}^{-1}(E(\hat{\theta}_{m_t})). \quad (2)$$

Here, $E(\cdot)$ is as defined in Equation 1, with the correspondence set \mathcal{C}_t fixed. Hence, the inverse Hessian is computed just with respect to the model parameter vector. There is no need to scale the inverse Hessian by the error variance because the error variance is included in the objective function.

The formation of the matching constraints plays an important role in (2). These constraints must realistically describe the information that is truly provided by a correspondence. To take an extreme and somewhat unrealistic example, suppose the points \mathbf{p}_i are sampled from a single, infinite line in image I_1 and matched to a corresponding infinite line in I_2 . Let the corresponding points found by ICP on the line be \mathbf{q}_i , and suppose just rotation and translation are being estimated. Then, if Euclidean distance constraints are used in (1), the covariance matrix will appear to be extremely stable, whereas if normal distance constraints (Section 2) are used, the

covariance matrix will be unstable. Clearly, the latter is correct because translation along the line is undetermined. This is the aperture problem in registration.

The Dual-Bootstrap ICP algorithm uses Σ_{m_t} in bootstrapping the model, and in bootstrapping the region. In the latter, Σ_{m_t} is applied to calculate the transfer uncertainty in mapping a point from I_1 to I_2 [33, Ch. 4]. Let point \mathbf{p} be an image location in I_1 and let $\mathbf{p}' = M_{m_t}(\hat{\boldsymbol{\theta}}_{m_t}; \mathbf{p})$ be the transformed location in I_2 . Computing the covariance of \mathbf{p}' requires the Jacobian of the transformation:

$$\mathbf{J}(\mathbf{p}) = \frac{\partial M(\hat{\boldsymbol{\theta}}_{m_t}; \mathbf{p})}{\partial \mathbf{p}}.$$

Combining this with Σ_{m_t} gives the covariance of the transformed point:

$$\Sigma_{\mathbf{p}'} = \mathbf{J}(\mathbf{p}) \Sigma_{m_t} \mathbf{J}(\mathbf{p})^T. \quad (3)$$

This equation may be generalized as required when the points are more than just coordinate locations.

3.4 Robust ICP

A robust version of the standard ICP algorithm is used as part of the Dual Bootstrap ICP algorithm. Recall that standard ICP alternates steps of matching and parameter estimation. The main innovations here are in robust parameter estimation and especially in error scale estimation.

In matching, the standard ICP technique is to find the closest feature point to $\mathbf{p}' = M_{m_t}(\hat{\boldsymbol{\theta}}_{m_t}; \mathbf{p})$, where \mathbf{p} is one of the feature points in \mathcal{P}_t selected from R_t . A variety of techniques, such as digital distance maps [6, 21] in 2D, octree splines [72] and z-buffering [1], may be used to accelerate this process [3, 60]. All of the matches are placed in the correspondence set \mathcal{C}_t for this iteration.

Given \mathcal{C}_t , the new estimate of the transformation parameters $\hat{\boldsymbol{\theta}}_{m_t}$ is computed by minimizing

$$E_t(\boldsymbol{\theta}_{m_t}) = \sum_{(\mathbf{p}, \mathbf{q}) \in \mathcal{C}_t} \rho(d(M_{m_t}(\boldsymbol{\theta}_{m_t}; \mathbf{p}), \mathbf{q})/\hat{\sigma}). \quad (4)$$

As discussed earlier, ρ is a robust “loss” function. Three robust loss functions are illustrated in Figure 5. Equation 4 may be solved using iteratively-reweighted least-squares (IRLS) [36], with weight function $w(u) = \rho'(u)/u$. The minimization process alternates weight recalculation using

a fixed parameter estimate with weighted least-squares estimation of the parameters. Levenberg-Marquardt techniques may also be used to minimize $E_t(\cdot)$.

The choice of loss functions is motivated by looking at the associated weight functions illustrated in Figure 5. The least-squares loss function has a constant weight, the Cauchy weight function descends and asymptotes at 0, while the Beaton-Tukey biweight function has a hard limit beyond which the weight is 0. The latter is important for rejecting errors due to mismatches. The details of the Beaton-Tukey biweight are

$$\rho(u) = \begin{cases} \frac{a^2}{6} [1 - (1 - (\frac{u}{a})^2)^3] & |u| \leq a \\ \frac{a^2}{6} & |u| > a \end{cases}$$

and

$$w(u) = \begin{cases} [1 - (\frac{u}{a})^2]^2 & |u| \leq a \\ 0 & |u| > a. \end{cases}$$

Using, $a \approx 4.0$ [36], means that correspondences producing errors larger than about 4 error standard deviations have no weight. Other loss functions sharing this hard-limit property could also be used.

This discussion shows why accurately estimating the error scale, σ , is crucial. Estimation of error scale is done for each set of correspondences at the start of reweighted least-squares. We use a technique called MUSE that automatically adjusts its estimate by determining the fraction of (approximately) correct matches [50, 51]. This is important because sometimes more than 50% of the feature points in R_t are mismatched. (An example of this occurs during the registration process shown in Figure 3 when R_t covers about half the overlap between images.) Let $r_j = |d(M_{m_t}(\hat{\boldsymbol{\theta}}_{m_t}; \mathbf{p}), \mathbf{q})|$ be the absolute error estimate for the j th correspondence using the current estimate $\hat{\boldsymbol{\theta}}_{m_t}$ of the transformation parameters. Let $r_{1:N}, r_{2:N}, \dots, r_{N:N}$ be a rearrangement of these values into non-decreasing order. Then for any k , $r_{1:N}, \dots, r_{k:N}$ are the k smallest errors. A scale estimate may be generated from $r_{1:N}, \dots, r_{k:N}$ as

$$\sigma_k^2 = \frac{\sum_{j=1}^k r_{j:N}^2}{C(k, N)},$$

where $C(k, N)$ is a computed correction factor. This factor makes σ_k^2 an unbiased estimate of

the variance of a normal distribution using only the first k out of N errors. The intuition behind MUSE is seen by considering the effect of outliers on σ_k^2 . When k is large enough to start to include outliers (errors from incorrect matches), values of σ_k^2 starts to increase substantially. When k is small enough to include only inliers, σ_k^2 is small and approximately constant. Thus, we can simply evaluate σ_k^2 for a range of values of k (e.g. $0.35N, 0.40N, \dots, 0.95N$), and choose the smallest σ_k^2 . To avoid values of k that are too small, we in fact take the minimum variance value of σ_k^2 , not just the smallest σ_k^2 . Details are in [50, Chapter 3].

3.5 Bootstrapping the Model

Increasing complexity models can and should be used as the bootstrap region, R_t , increases in size and includes more constraints. Changing the model order must be done carefully, however. Switching to higher order models too soon causes the estimate to be distorted by noise. Switching too late causes modeling error to increase the error scale, $\hat{\sigma}$, and causes misalignments on the boundaries of R_t . Both of these cause mismatching. An example of the latter is shown in Figure 6. To select the correct model for each bootstrap region, statistical model selection techniques are applied.

Automatic model selection is a well-studied problem [7, 75], and experimental analysis shows that none of the techniques is ideal [7]. All techniques choose the model that optimizes a trade-off between the fitting accuracy of high-order models and the stability of low-order models. The current Dual-Bootstrap ICP model selection criteria is adapted from [7]. The expression is

$$\frac{d_m}{2} \log 2\pi - \sum_i w_i r_i^2 + \log \det(\Sigma_\theta), \quad (5)$$

where d_m is the degrees of freedom in the model, $\sum_i w_i r_i^2$ is the sum of the robustly-weighted transformation errors, and $\det(\Sigma_\theta)$ is the determinant of the parameter estimate covariance matrix. Notice that if Σ_θ is not full-rank, then the third term goes to $-\infty$.

In the model bootstrap step of the Dual-Bootstrap ICP algorithm, expression (5) is evaluated for each model, M_1, \dots, M_f , using the fixed set of matches \mathcal{C}_t determined by robust ICP in iteration t . For each model, iteratively-reweighted least-squares estimation is applied, and the final weights, error residuals, and computed covariance matrix are used to evaluate (5). The model yielding the largest value is taken as the new model, $\mathbf{M}_{m_{t+1}}$.

One step that could be added is to allow rematching with different models prior to model selection — in other words to run full robust ICP for each model. If there is a smooth transition between models, which means that the switch in models in a fixed bootstrap region, R_t , does not dramatically change the mapped locations of points in R_t , then this is unlikely to be necessary. This issue is discussed further in Section 6.

The final issue in bootstrapping the model is that an appropriate set of models must be chosen. This is an application-specific consideration, but two concerns must be addressed. First, the models should be based on geometrically-plausible approximations to the image-wide transformation. Otherwise, the added degrees of freedom can lead to improper distortions of the transformation in response to mismatches and noise. Second, there should be a gradual increase in the precision of the models as applied in the given application. Otherwise, the algorithm may stay with a lower-order model too long (Figure 6) or switch to a higher-order model too early.

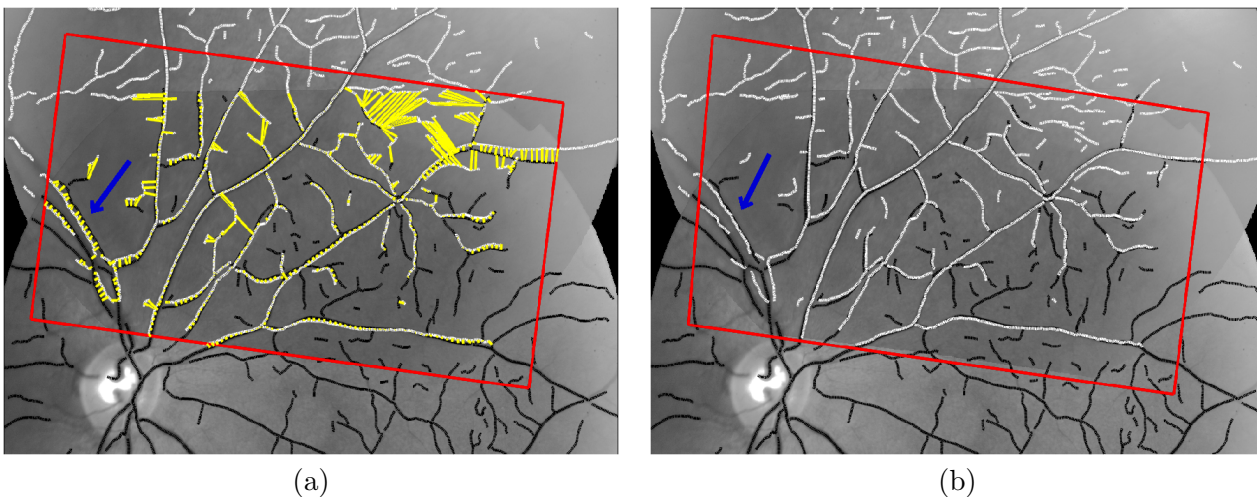


Figure 6: An example using retinal image registration showing an example of mismatching at the border of the region if the change in model order occurs too late. In (a) a similarity transformation is used for a large bootstrap region, and the vascular structure on the left border (indicated by the arrow) is mismatched. (Matches are shown by the yellow line segments.) As seen in (b) this eventually causes convergence to the incorrect final transformation estimate. In our actual implementation this mistake does not happen because bootstrap model selection switches to a higher-order model before R_t grows to include this area of the image.

3.6 Bootstrapping the Region – Region Expansion

The bootstrap region is expanded based on transfer error (Section 3.3) for points on the boundary of R_t , with lower transfer error leading to faster bootstrap region growth. In the current

algorithm, region R_t is rectangular. Each side of R_t is expanded independently, allowing more rapid expansion where there is less ambiguity (see Figure 3). For each segment, let \mathbf{u} be the point in the center of the segment that defines the side (see Figure 7 for a depiction of R_t for two-dimensional images), let \mathbf{d} be the outward normal at \mathbf{u} , let \mathbf{u}' be the transformed location of \mathbf{u} based on the current model and estimate, and let $\Sigma_{\mathbf{u}'}$ be the covariance matrix for this point (Equation 3). Note that all of these estimates are computed in a coordinate system that is aligned with the center of R_t . The uncertainty of the transformation of \mathbf{u} in outward direction \mathbf{d} , is

$$U(\mathbf{u}, \mathbf{d}) = \max(1, \mathbf{d}^T \Sigma_{\mathbf{u}'} \mathbf{d}).$$

The change in location \mathbf{u} is

$$\left(\frac{|\mathbf{u}^T \mathbf{d}| \beta}{U(\mathbf{u}, \mathbf{d})} \right) \mathbf{d}.$$

Here, β determines the maximum expansion rate at each side. The lower bound of 1 in $U(\mathbf{u}, \mathbf{d})$ prevents region growth that is too rapid. Clearly, as $U(\mathbf{u}, \mathbf{d}) \rightarrow \infty$, the expansion of \mathbf{u} goes to 0. The new region R_{t+1} is the rectangle (in two-dimensions) formed by the expanded sides. The growth parameter β is set based on the desired maximum growth rate. For example, setting β to $\sqrt{2} - 1$ ensures that R_t does no more than double in area in each iteration.

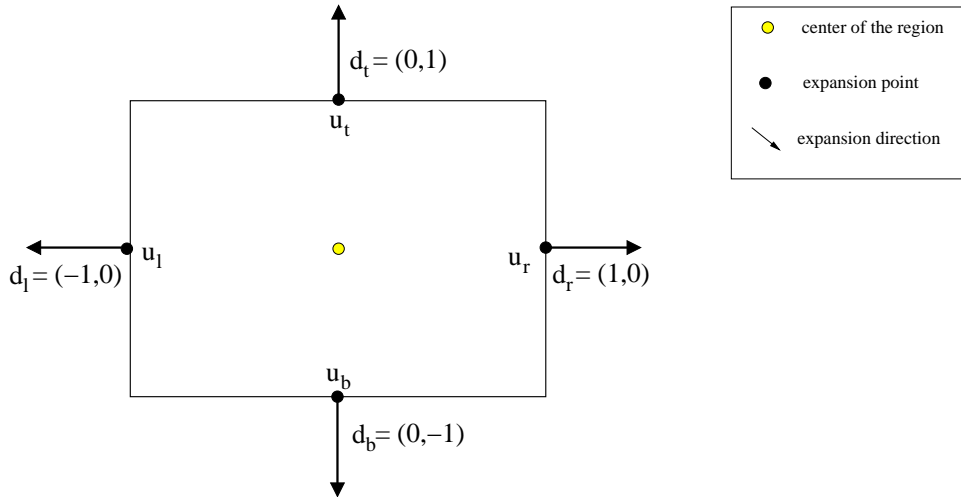


Figure 7: The bootstrap region is expanded by moving out perpendicular to each side. In directions where the estimate is more stable, expansion is faster.

4 Retinal Image Registration Using Dual-Bootstrap ICP

A major consequence of the sophisticated minimization technique of the Dual-Bootstrap ICP algorithm is that the initial conditions from which it can converge are substantially weakened. We have described it as requiring just a “toe hold” on an accurate alignment. This means that the initial estimate must be accurate enough to generate (mostly) correct correspondences in the bootstrap region in the first iteration.

For retinal image registration, this is crucial. In high-quality images of healthy retinas, many landmarks are available to initialize matching. In lower quality images or in images of unhealthy retinas, fewer landmarks are prominent. Therefore, we implement the Dual-Bootstrap ICP algorithm in retina image registration to start from a similarity transformation initialized by matching a single pair of landmarks or by matching two pairs of landmarks. The algorithm tests many different initial correspondences, allowing the Dual-Bootstrap ICP to converge for each. It stops and accepts as correct a registration having a stable transformation and a highly accurate alignment. As we will see, the complete algorithm has nearly flawless performance.

Here are some of the important implementation details:

Point sets: As discussed earlier, the points (Figure 1) are the blood vessel centerlines and landmarks — branches and cross-over points of blood vessels — extracted using an exploratory algorithm described in [8, 66, 27]. The centerline points are characterized by location, orientation and width, while the landmarks are characterized by their center location, the orientation of the blood vessels that meet to form them, and the widths of these vessels (Figure 8).

Invariants: Matches between two landmarks, one in each image, or between pairs of landmarks in each image are generated by computing and comparing invariants [4, 53]. Invariants for a single landmark are blood vessel width ratios and blood vessel orientations (Figure 8), giving a five-component invariant signature vector. The invariant signature of a set of two landmarks is a six-component vector (Figure 9). The line segment drawn between the two landmarks forms an axis, and the orientation of each of the three landmark angles is computed with respect to this axis, giving the six components. The combination of two types of invariant is used because the single-landmark invariants are the limit of what can

be accomplished by matching landmarks, whereas the pair-invariants allow more flexibility to changes in orientation and mismeasurement of blood-vessel width.

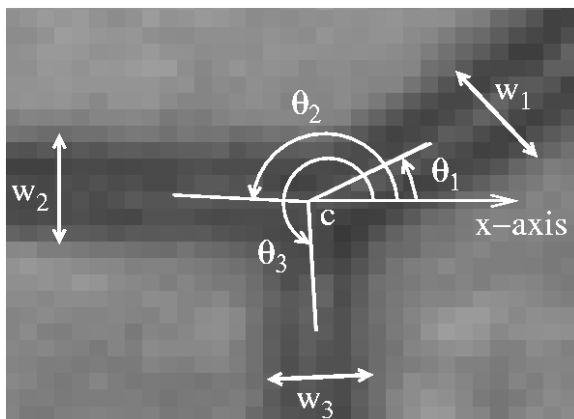


Figure 8: A landmark is characterized by a center location \mathbf{q}_c , the orientations ϕ_j of the three blood vessels that meet to form it and the widths w_j of the blood vessel. The traced vascular centerline points are illustrated by the small, hollow circles on the leftmost vessel. Differences in orientations and the ratios of the blood vessel widths are invariant to rotation, translation and scaling of the image — a similarity transformation. The orientations themselves are invariant to translation and scaling.

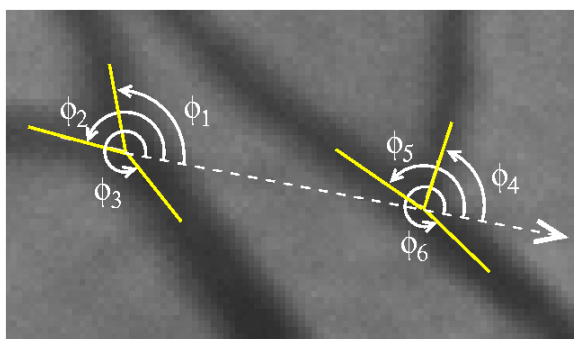


Figure 9: The invariant signature of a pair of landmarks. The line segment drawn between the two landmarks forms an axis, and the orientation of each of the three landmark angles is computed with respect to this axis, giving a six-component signature vector.

Initial matching: The invariant signature vectors for one- and two-landmark sets are computed separately for each image, I_1 and I_2 , and then matched (each set separately). At least one match is found for each signature vector. Additional matches are determined when the Mahalanobis distance between signature vectors is within a chi-squared uncertainty bound. Each signature match produces a set of one or two landmark correspondences. These sets are ordered for testing by chi-squared confidence levels. For each set, a similarity

transformation is computed which generates the initial transformation.

Iterative matching: The matching constraints during iterative minimization of Dual-Bootstrap ICP are point-to-line matches (illustrated in Figure 4). To facilitate matching, the centerline points are stored in a digital distance map [6, 21]. The initial bootstrap region, R_1 , around a single landmark correspondence is (somewhat arbitrarily) chosen to be a square whose width is 10 times the width of the thickest blood vessel forming the landmark. The initial bootstrap region around a pair of landmarks is the smallest rectangle enclosing what would be the individual initial regions. Early in the minimization process, the matching constraints are generated from the boundaries of the blood vessels in R_t , yielding two constraints from each point. This helps constrain the magnification in the similarity transformation. As the region is grown, a switch is made to matching just centerline points, because these are more stable. The switch is made when the similarity transformation parameter estimate is sufficiently stable based on centerline matches alone.

Transformation Model Set: Four transformation models have been considered: similarity, affine, “reduced quadratic” and quadratic [9, 11] as illustrated in Table 1. All but the reduced quadratic, which is new here, have been used in retinal image registration before. The reduced quadratic can be derived as an approximation to the change induced in a weak-perspective camera when a sphere rotates about its center. As seen in the table, it has the same number of degrees of freedom as the affine model, but is much more accurate. The affine model is in fact problematic. Its extra degrees of freedom as compared to the similarity model allow shearing, which is unrealistic for retinal imaging. In practice, we do not use the affine model, although the model selection technique would automatically ignore it anyway.

Termination Criteria: The termination criteria are straightforward. For a single initial estimate, the Dual-Bootstrap ICP algorithm stops bootstrap region growth when the region, R_t , encompasses the apparent area of overlap between the two images. From then on only the model selection and robust ICP process are applied until they converge as well. If the median matching error of the resulting transformation is sufficiently low (threshold of 1.5 pixels, as determined empirically [11]) and the quadratic transformation parameters are sufficiently stable, this transformation is accepted as correct. In addition, purely for effi-

Transformation	Equation	DoF	Accuracy
Similarity	$\mathbf{q} = \begin{pmatrix} \theta_{11} & \theta_{12} & \theta_{13} & 0 & 0 & 0 \\ \theta_{21} & -\theta_{13} & \theta_{12} & 0 & 0 & 0 \end{pmatrix} \mathbf{X}(\mathbf{p})$	4	5.05 pixels
Affine	$\mathbf{q} = \begin{pmatrix} \theta_{11} & \theta_{12} & \theta_{13} & 0 & 0 & 0 \\ \theta_{21} & \theta_{22} & \theta_{23} & 0 & 0 & 0 \end{pmatrix} \mathbf{X}(\mathbf{p})$	6	4.58 pixels
Reduced quadratic	$\mathbf{q} = \begin{pmatrix} \theta_{11} & \theta_{12} & \theta_{13} & \theta_{14} & 0 & \theta_{14} \\ \theta_{21} & -\theta_{13} & \theta_{12} & \theta_{24} & 0 & \theta_{24} \end{pmatrix} \mathbf{X}(\mathbf{p} - \mathbf{p}_0)$	6	2.41 pixels
Quadratic	$\mathbf{q} = \begin{pmatrix} \theta_{11} & \theta_{12} & \theta_{13} & \theta_{14} & \theta_{15} & \theta_{16} \\ \theta_{21} & \theta_{22} & \theta_{23} & \theta_{24} & \theta_{25} & \theta_{26} \end{pmatrix} \mathbf{X}(\mathbf{p})$	12	0.64 pixels

Table 1: The set of transformation models used in retinal image registration. To clarify notation in the equations, $\mathbf{p} = (x, y)^T$ is an image location in I_1 and $\mathbf{q} = (u, v)^T$ is the transformed image location in I_2 . $\mathbf{X}(\mathbf{p}) = (1, x, y, x^2, xy, y^2)$ is a second-order basis. Finally, \mathbf{p}_0 is the center of the region of overlap between the images. This is required in the reduced quadratic model, but is used in practice in all models. In addition to the formulations, the table also shows the degrees of freedom (DoF) in each model and the average alignment error on 1024×1024 images.

ciency reasons, estimated transformations that are clearly incorrect are rejected early, prior to convergence, if either of the following (heuristic) conditions holds: (a) the covariance matrix of the current estimate, Σ_{m_t} , is unstable (as measured by its condition number), (b) the estimate $\hat{\theta}_{m_t}$ is too uncertain for bootstrap region R_t to expand when the quadratic model has been chosen.

5 Experimental Analysis

This section presents the results of a large number of experiments using the Dual-Bootstrap ICP in retinal image registration. The presentation illustrates the nearly flawless performance of the algorithm and then illustrates the importance of each major component of the dual bootstrapping process.

5.1 Data and Analysis

The performance of the algorithm is demonstrated on two groups of image data sets. One contains images from 18 different healthy eyes, with 15-25 images in each set. These images

show a wide range of views of each retinal fundus, and some pairs of images of the same eye have no overlap whatsoever. The second data set contains images from 40 different eyes with various pathologies, yielding 300 image pairs. Some of these pairs were taken at the same time, while others were taken with time differences of months or even years. Results are presented for the two data sets separately because the second, “pathology” set is more challenging, but much smaller. Figure 3 illustrates the Dual-Bootstrap ICP algorithm on images of an unhealthy retina taken at the same sitting. Figure 10 illustrates the algorithm on a pair of images taken two months apart. Figure 11 illustrates the algorithm on a pair of images of a healthy retina. All images in our dataset are 1024×1024 pixels.

Measuring performance requires a means of validation, preferably ground truth. Manually generated ground truth is extremely difficult for such a large data set, and our experience is that this is less accurate than automatic registration anyway. Fortunately, we have a multipart alternative strategy. First, for the set of images from any given eye, we can jointly align all images, including pairs that have little or no overlap, using a joint, multi-image mosaicing algorithm [10]. This uses constraints generated from pairwise registration, and produces quadratic transformations (see Table 1) between all pairs of images, even ones that failed pairwise registration. (Viewing the set of images as nodes in an undirected graph and the successful pairwise registrations as edges in the graph, the only requirement is that the graph be connected.) We then manually validate the resulting transformations by viewing the alignment of the images. It is important to note that no image in our data set was left out by this technique! We therefore have “correct” transformations for all possible image pairs in our data set. The alignment error averages less than 1 pixel.

Having these validated transformations is the basis for the crucial next step: developing approximate upper bounds on the performance of point-based registration. Taking the set of vascular landmarks and centerline points for each image as given and fixed, we ask the question, “what is the best possible performance of an ICP-like registration algorithm?” Referring back to the objective function in Equation 1, for any pair of images we can start from the “correct” transformation and therefore find an excellent approximation to the correct set of matches (again, with the point sets fixed). From there we can determine the covariance of the transformation estimate. If the condition number of this matrix indicates that the transformation is sufficiently stable, we say that a point-based registration between these image pairs is possible. Denoting

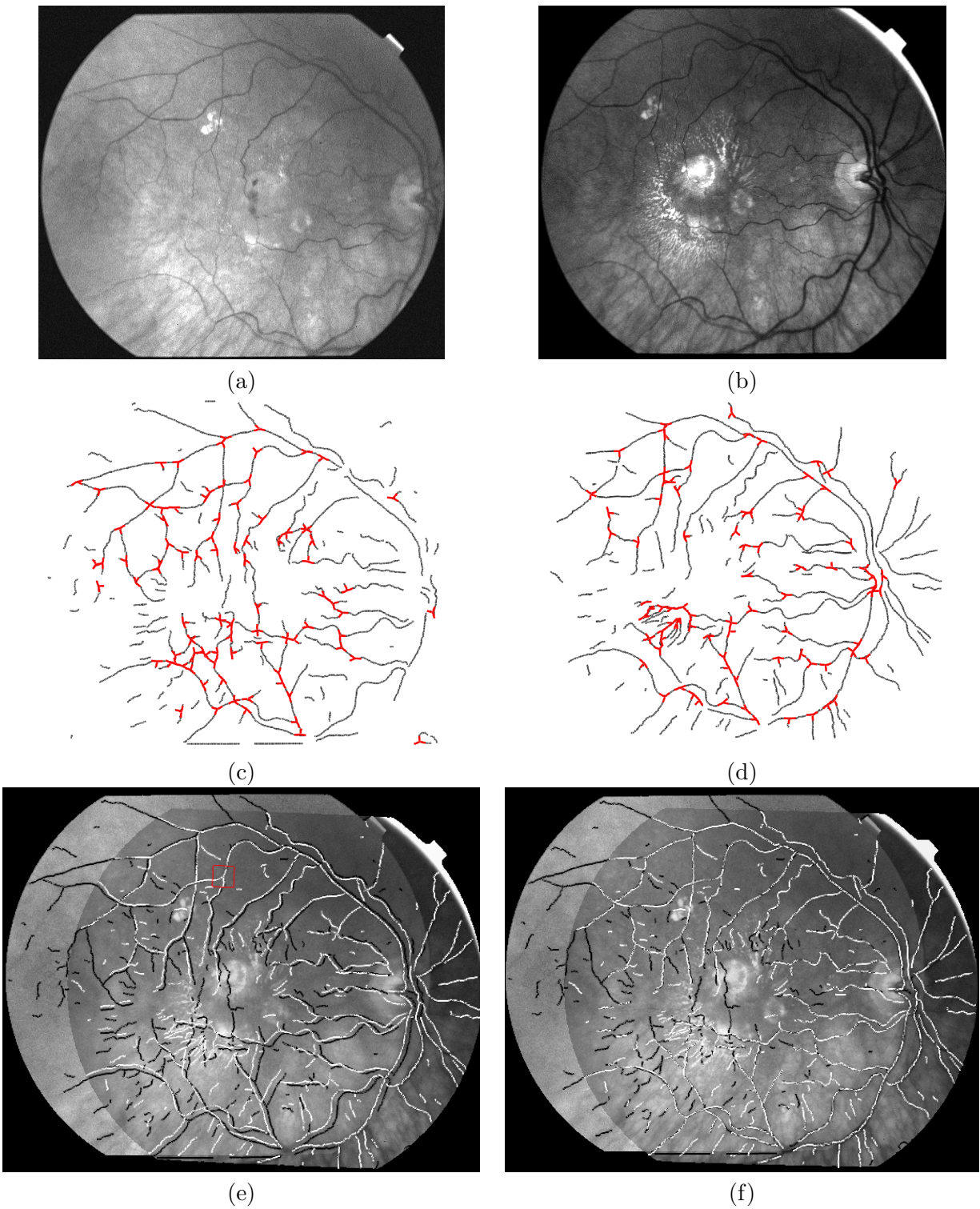


Figure 10: Illustrating the Dual Bootstrap ICP retinal image registration algorithm on a pair of images from an unhealthy eye taken 2 months apart. The images are shown in panels (a) and (b). The vascular centerline points and landmarks are shown in (c) and (d). Panel (e) shows the alignment of the two images based on a locally-correct initial transform. Panel (f) shows the final global alignment estimated by the Dual-Bootstrap ICP algorithm starting from this initial estimate.

these pairs as \mathcal{M}_h and \mathcal{M}_p for the healthy and pathology sets respectively, we can measure the success rate of our algorithm as a percentage of the sizes of these two sets. This is our first performance bound. Our second, and tighter bound, restricts \mathcal{M}_h and \mathcal{M}_p by eliminating image pairs that have no common landmarks. We can discover this by using the “correct” transformations to find corresponding landmarks. We refer to the reduced sets as \mathcal{M}_h^1 and \mathcal{M}_p^1 . Success rates on these sets separates performance of initialization from performance of the iterative minimization of the Dual-Bootstrap ICP algorithm and gives an idea of how well it does given a reasonable starting point. The cardinalities of these sets are $|\mathcal{M}_h| = 5,753$, $|\mathcal{M}_p| = 369$, $|\mathcal{M}_h^1| = 5,611$, and $|\mathcal{M}_p^1| = 361$.

5.2 Overall Performance

The first and most important measure of overall performance is the success rate — the percentage of image pairs for which a correct (within 1.5 pixels of error) transformation estimate is obtained.

This is summarized in the following table for the healthy-eye and pathology-eye datasets:

	all pairs	one landmark pairs
healthy — \mathcal{M}_h (%)	97.0	99.5
pathology — \mathcal{M}_p (%)	97.8	100

Table 2: Overall success rate of the Dual-Bootstrap ICP retinal image registration algorithm on healthy-eye and pathological-eye images. The first column, labeled “all pairs”, is for all “correct” image pairs — the sets \mathcal{M}_h and \mathcal{M}_p . The second column, labeled “one landmark”, is for all “correct” image pairs having at least one common landmark — the sets \mathcal{M}_h^1 and \mathcal{M}_p^1 .

These numbers are extremely high, and show virtually flawless performance of the overall registration algorithm, including initialization, and the Dual-Bootstrap ICP algorithm in particular. (By comparison, our previous retinal image registration algorithm [11], which was based on matching landmarks and their surroundings, was 67.1% for the healthy-eye set, \mathcal{M}_h .) The few failures are due to having few common landmarks or a combination of sparse centerline trace points and low overlap. This is illustrated using a bar chart in Figure 12. To reinforce this, for image pairs that overlap in at least 35% of the pixels and have at least one correspondence, *there were no failures*. This involved over 4000 image pairs. An example pair for which the algorithm failed is shown in Figure 13. These images have 32% overlap and one common landmark. This performance means that the overall algorithm is ready for large-scale clinical testing and

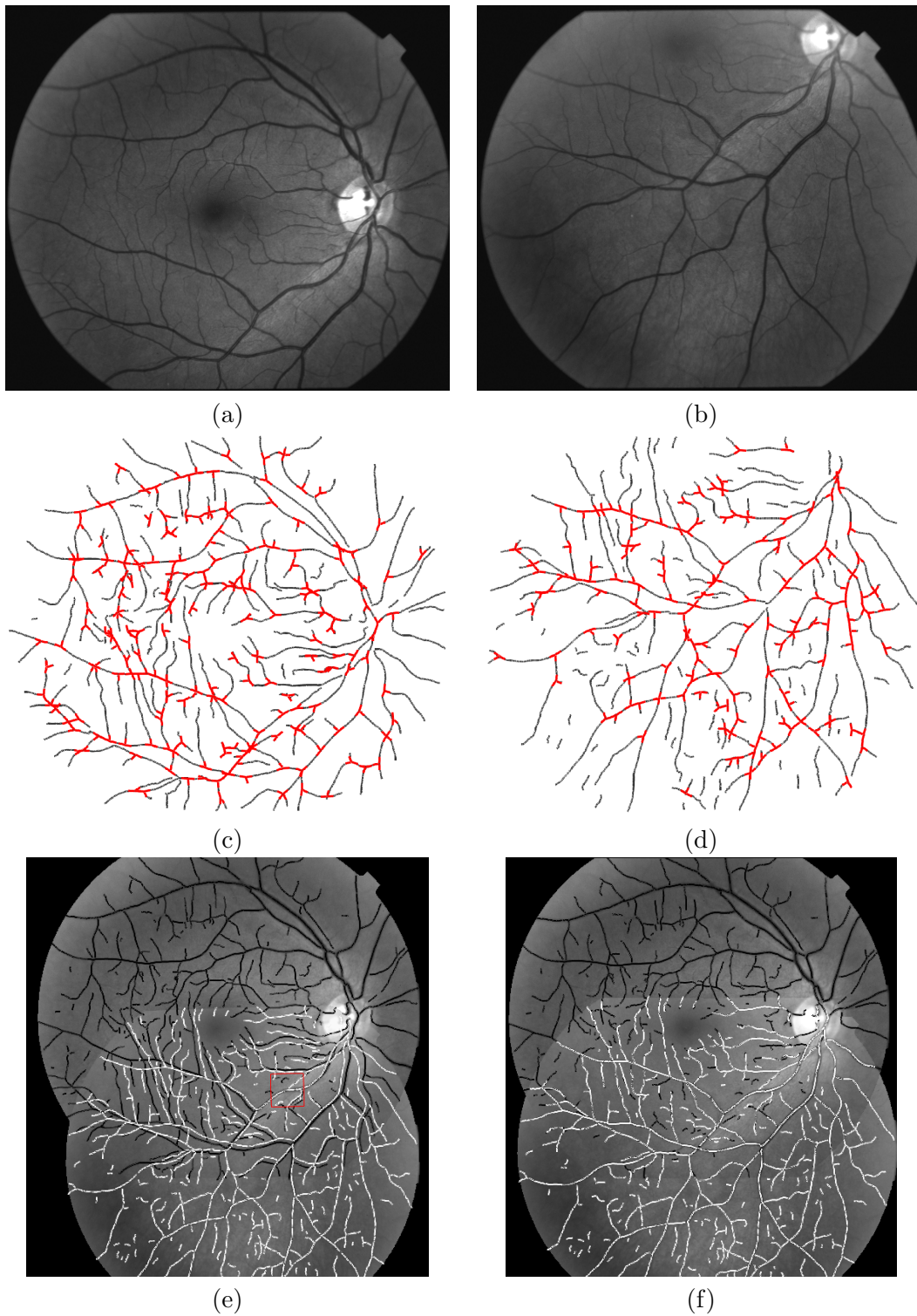


Figure 11: Illustrating the Dual Bootstrap ICP retinal image registration algorithm on a healthy-eye image pair that has 50% overlap. The images are shown in panels (a) and (b). The vascular centerline points and landmarks are shown in (c) and (d). Panel (e) shows the alignment of the two images based on a locally-correct initial transform. Panel (f) shows the final global alignment estimated by the Dual-Bootstrap ICP algorithm starting from this initial estimate.

application to change detection and visualization.

As an aside, the apparently counter-intuitive result that the pathology data set has higher success rate is explained by the pathology image pairs having higher overlap, on average. The healthy-eye images were deliberately taken to obtain complete views of the fundus, whereas the pathology-eye images were taken to capture the diseased region(s).

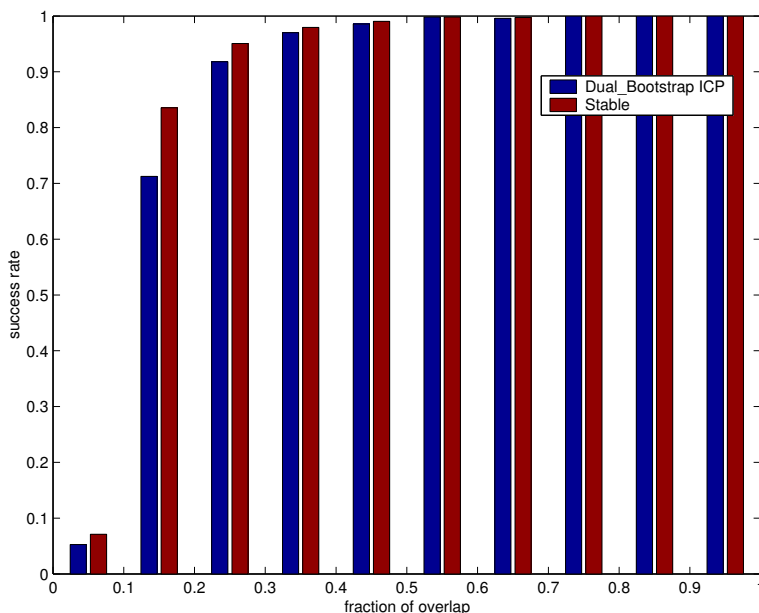


Figure 12: Plotting the percentage of successful retinal image registrations as a function of overlap between images. The plots include all image pairs, not just those for which a stable transformation is available. The percentage for the Dual-Bootstrap ICP based algorithm and the percentage of stable transformation are both shown for each interval. When the two heights are equal, 100% success was obtained by Dual-Bootstrap ICP. Plotting the results this way shows the overall difficulty in obtaining enough information to register at extremely low overlaps. Even here, however, the success rate of the algorithm nearly matches the best possible for a fixed set of points.

As a final indication of the overall algorithm, here is a summary of some additional experimental details:

- Using matching of single landmarks between images resulted in a 96.7% success rate, whereas matching pairs of landmarks from each image resulted in a 90.4% success rate. Since the overall performance was 97.0%, the combination of both did improve performance, although single landmark matching alone was nearly as effective.
- The growth rate parameter, β , which is the only tuning parameter, had little effect on the overall success rate of the algorithm. We tested values of β ranging from 0.25, which

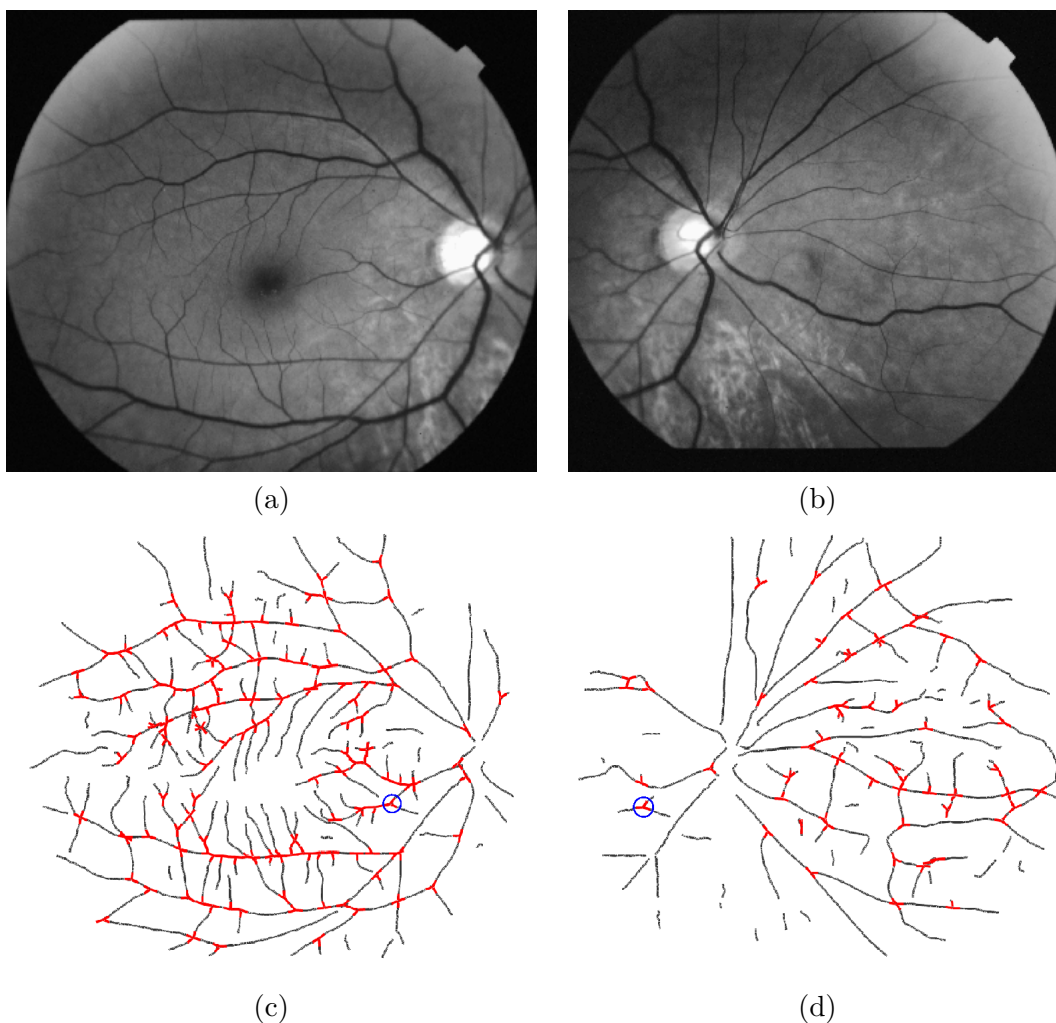


Figure 13: Two images having 32% overlap and one common landmark where the Dual-Bootstrap ICP retinal image registration algorithm failed. The images are shown in (a) and (b) and the landmarks and traces are shown in (c) and (d) with the common landmark circled. There are significant missing traces in (d). This problem has been fixed in the latest version of the tracing algorithm.

corresponds to growing the area by at most a factor of 1.56 per iteration, to 1.0, which corresponds to maximum area growth factor of 4 per iteration, without changing the success rate of the algorithm. Values of β beyond 1.0 caused a very gradual reduction in the effectiveness, with $\beta = 8$ still having a 96.6% success rate on \mathcal{M}_h .

- The value of $\beta = \sqrt{2} - 1$, which corresponds to at most doubling the area in each iteration, resulted in a median of 10 bootstrapping iterations. Larger values of β caused fewer iterations. For example, $\beta = 1.0$ caused a median of 6 iterations.
- Over the entire dataset, including both healthy and pathology eye images, the median

number of matches tried before the algorithm succeeded was 1 and the average was 5.5. The large difference between the median and the average is caused by a small number of image pairs that required an extremely large number of initial estimates before success. The worst was 746.

- The execution time required by the algorithm varied considerably with the number of initial estimates required before success. On a 933MHz Pentium III computer running FreeBSD, the median time was 5 seconds. Much of the time was taken in building the matching database for pairs. Eliminating the use of pairs reduced the median time to 3.5 seconds.

5.3 Evaluation of Dual-Bootstrapping

Given the nearly flawless performance of our retinal image registration algorithm, the crucial issue is how much of it is due to the Dual-Bootstrap ICP formulation. We can address this by removing each of the three major components from the Dual-Bootstrap algorithm in turn: region growth, model selection, and robust estimation. The results are summarized in Table 3 and discussed as follows.

Region growth: Removing bootstrap region growth means that the initial similarity estimate was used to generate image-wide correspondences, as in standard ICP, and then the algorithm was run with no bootstrap region growth. Robust estimation and model selection were still used, although the latter played a minor role. The success rates were 89.4% and 82.4%. The drop is most significant — 16% — in the pathology set, which substantiates the need for the Dual-Bootstrap algorithm on more difficult images. As interesting asides, without bootstrap region growth, twice as many initial matches were tried, and pairs of landmark correspondences were used 26% more often.

	No region growth	No model selection	No robustness
Healthy \mathcal{M}_h (%)	89.4	84.7	39.0
Pathology \mathcal{M}_p (%)	82.4	80.5	12.5

Table 3: Success rates of retinal image registration when each of the three main component of the Dual-Bootstrapping ICP algorithm was removed separately: region growth, model selection, and robust estimation. These are significantly lower than the 97.0% and 97.8% numbers for the overall algorithm.

Model selection: When bootstrap model selections was eliminated, a single model was used for the entire process of bootstrap region growth and robust ICP refinement. The natural model to use is the quadratic. The first set of quadratic parameters was estimated from the correspondences in the initial bootstrap region. Using the quadratic model only led to a low success rate, as shown in Table 3. On the other hand, when we initialized an intermediate model — the reduced quadratic — from the initial bootstrap region, allow the algorithm to run to convergence, and then switch to the quadratic transformation, performance was much better: 94.1% on the healthy-eye set and 94.6% on the pathology-eye set. The reason for this improvement is that the reduced quadratic is relatively accurate without requiring too many constraints. Still, however, model selection is important for the most difficult image pairs. Using the similarity transformation for bootstrap region growth is worse than reduced quadratic — 91.7% and 93.0% — but not as bad as the quadratic.

Robust estimation: At first thought, the dual-bootstrapping process might seem to eliminate the need for robust estimation, because the growth process ensures reliable correspondences. This is not true, of course. By replacing the Beaton-Tukey ρ function with a least-squares ρ function, the performance became dramatically worse (Table 3). This is because mismatches are still clearly possible. If matching was limited to distances based on a combination of modeling and transfer error (as will be discussed in detail in Section 6), then robust estimation would not be as important. But, clearly this would be its own form of robust estimation and use what amounts to a truncated quadratic. Finally, further experiments showed that the use of MUSE scale estimator over a more common estimator such as median absolute deviation [57] improved the effectiveness of the overall algorithm (93.3% and 88.3%).

Clearly, these experiments show that all components of the Dual-Bootstrap algorithm are important, with importance increasing substantially for the more difficult pathology eye data set.

6 Discussion

The Dual-Bootstrap ICP algorithm has been described in general terms and then implemented and tested in a complete technique for retinal image registration. The results far outperform any

current algorithm for this specific application. We have claimed that the algorithm is broadly useful, however. To establish this, it is important to compare the Dual-Bootstrap ICP algorithm (a) to other techniques that have been used to improve ICP and (b) more generally to other point-based registration algorithms. It is also important to establish mathematically the conditions under which it should be used rather than standard (but robust) ICP. Finally, we must consider circumstances under which the algorithm might fail.

6.1 Comparison to Related Techniques

We compare the Dual-Bootstrap ICP algorithm to five classes of techniques that have been used to improve ICP:

- Several published papers have used genetic algorithms and simulated annealing for a broad search of the landscape of possible parameter estimates [5, 13, 15, 45]. Closest point correspondences are used to evaluate each parameter estimate, with eventual application of ICP for final refinement. The Dual-Bootstrap ICP makes such coarse search techniques unnecessary if locally-accurate bootstrap region estimates can be obtained. Indeed, for the retinal image registration problem our algorithm appears to be far better than currently published techniques using genetic algorithms and simulated annealing [47, 56], based on the results reported in the papers.
- When a significant number of distinctive features can be obtained, geometric hashing is an efficient, reliable alignment method, especially for similarity transformations [30]. Clearly, this assumes much more about the quality of the data than the Dual-Bootstrap ICP algorithm.
- By enriching the feature set, matching can be improved, both prior to ICP and during ICP [44, 65, 74]. Both lead to a broader domain of convergence. This approach is complementary to the Dual Bootstrap ICP algorithm, which is designed to maximize the effectiveness of registration for a given, fixed registration point (feature) set. Enriched features and Dual-Bootstrap ICP can be used in combination.
- Multiresolution techniques have been used for many years in registration [24, 62, 63] and a variety of other applications [2]. Multiresolution works from coarse descriptions of the

entire image / data set and (perhaps) simpler models, using the results at coarse resolutions as starting points for finer resolution refinement. By contrast the Dual-Bootstrap ICP algorithm, together with appropriate initialization techniques, takes a local-to-global approach, focusing on small regions of the data first and then expanding to cover the entire data set. The Dual-Bootstrap ICP algorithm could be combined with multiresolution methods by applying it at the coarsest resolution.

- Robust techniques based on minimal subset random-sampling have been used for difficult registration and transformation estimation problems [33, 76, 77, 79], including applications of ICP [13, 46]. The difference that the Dual-Bootstrap ICP algorithm offers is important. Minimal subset random sampling [26, 58] requires a sufficient set of correspondences to generate a full model. When using the Dual-Bootstrap ICP algorithm, a much weaker initial model may be used, with fewer initial correspondences. This implies that the Dual-Bootstrap ICP algorithm can succeed where minimal subset random sampling fails.
- The final comparison is to the robust point matching (RPM) algorithm [17]. This uses a soft assignment of point correspondences, smoothing-spline transformations, and deterministic annealing to align point sets. Thus, it globally considers all matches and gradually refines the matches and the spline transformation parameters simultaneously. This contrasts with the Dual-Bootstrap ICP local (small region) to global (large region) refinement with gradual incorporation of more matches. Intuitively, therefore, the Dual-Bootstrap ICP approach seems more applicable to situations where information in small data regions provides a “toe-hold” on the alignment. Still, because the two algorithms have been used in very different contexts, further evaluation, perhaps on an experimental test-bed, is needed.

6.2 Utility

Since the ICP algorithm and its variants have been used successfully in a variety of applications, it is important to address the issue of when the more sophisticated Dual-Bootstrap ICP should be used instead. The answer is that it depends on the quality of the data, the structural complexity of the data, and the accuracy of the initial model and parameter estimates. The following sketches an analysis method to indicate when the Dual-Bootstrap ICP should be considered.

Suppose $\hat{\theta}_0$ is an initial parameter estimate obtained using initial model M_0 . Suppose Σ_0 is

the associated parameter estimate covariance matrix. In applying the standard ICP algorithm, all points $\mathbf{p} \in \mathcal{P}$ throughout the entire image (see Equation 1) are mapped from I_1 to I_2 based on this initial estimate. Our goal is to calculate the uncertainty of this mapping, based on both the modeling error and the transfer error for this initial estimate, and relate this to the structure of the data.

In order to determine the modeling error, let $\bar{\boldsymbol{\theta}}_0$ be the optimal estimate based on the initial model M_0 , and let $\bar{\boldsymbol{\theta}}_f$ be the optimal estimate based on the true/final model M_f . (Optimality here is taken in an asymptotic sense of an estimate from a large number of correct, noise-free correspondences.) Then, the modeling error at point \mathbf{p} is

$$e_m(\mathbf{p}) = d(M_0(\bar{\boldsymbol{\theta}}_0; \mathbf{p}), M_f(\bar{\boldsymbol{\theta}}_f; \mathbf{p})).$$

This is the distance between optimally mapping a point based on the initial and final models. Clearly, if the initial and final models are the same, $e_{\mathbf{p}} = 0$.

In order to obtain the transfer error, let $\mathbf{p}' = M_0(\bar{\boldsymbol{\theta}}_0; \mathbf{p})$ be the transformation of $\mathbf{p} \in \mathcal{P}$. Referring back to Equation 3, the transfer error covariance matrix of \mathbf{p}' is

$$\boldsymbol{\Sigma}_{\mathbf{p}'} = \mathbf{J}(\mathbf{p}) \boldsymbol{\Sigma}_0 \mathbf{J}(\mathbf{p})^T.$$

Let $\sigma_{\mathbf{p}}^2$ be the maximum eigenvalue of $\boldsymbol{\Sigma}_{\mathbf{p}'}$. This gives the maximum transfer error variance in any direction at \mathbf{p}' . Assuming some reasonable multiplier on the standard deviation, such as $\mu = 2.5$, the upper bound on the transfer error of point \mathbf{p} due to uncertainty in the initial estimate is

$$e_t(\mathbf{p}) = \mu\sigma_{\mathbf{p}}.$$

Finally, the combined modeling and transfer error at point \mathbf{p} can then be defined as,

$$e(\mathbf{p}) = e_{\mathbf{p}} + \mu\sigma_{\mathbf{p}}$$

and the maximum error can be defined as

$$e_0 = \max_{\mathbf{p} \in \mathcal{P}} e(\mathbf{p}).$$

This may be interpreted by comparing e_0 against the structure of the data. If e_0 is larger than or even comparable to the distance between different geometric structures in the data — different blood vessels, different nerve fibers, different layers of the brain, different surfaces of a complicated object — then there is substantial potential for ICP mismatches. In this case, the Dual-Bootstrap ICP should be used in place of “standard” ICP.

Before ending this section, we offer a slightly different view on the utility of the Dual-Bootstrap ICP algorithm. Because it works robustly from only a “toe-hold” on the alignment between two datasets, it reduces the requirements on initialization. This can lead to a new way of thinking about approaching a registration or alignment problem. Less cleaning and prefiltering of the data is needed and more aggressive feature extraction and initialization techniques can be applied. This could lead to new methods and new successes on previously difficult registration or even recognition problems.

6.3 Potential Failures

Two conditions where the Dual-Bootstrap ICP algorithm may fail to converge following a locally correct initialization should be mentioned:

- This first may occur when the transition between models is not captured by the matching constraints generated by a low-order model. A simple, artificial example is registering two rectangles that have a significant scaling between them by starting at a single corner and using a Euclidean transformation (rotation and translation, no scale). Only when the bootstrap region grows large enough to include a second corner (third side) are constraints available to estimate scale. At this point the implicit scale (1.0) of the Euclidean transformation may be too far off of the true similarity transformation scale for correct matching.
- A second condition is when each data set has two or more geometrically separated clusters and the initial transformation is estimated only in a single cluster. As the gap between clusters grows, the transfer error will grow with it, potentially leading to mismatches when the bootstrap region R_t grows to include a second cluster.

While both examples are artificial, they do help to illuminate the Dual-Bootstrap method further. The first case shows that taking the idea of weak initial estimates too far can be problematic,

especially if it ignores information, such as clean corners, available in the data. If such a circumstance were to occur in the data, then a more sophisticated method of transitioning between models would be needed. The second case has actually appeared in rough form in our retinal image registration experiments due to a large region of missing data. In such circumstances, the use of accurate models becomes crucial, and this led to the discovery and introduction of the reduced quadratic transformation.

7 Conclusions

We have introduced and applied a new generalization of the Iterative Closest Point (ICP) algorithm. The Dual-Bootstrap ICP algorithm starts from an initial estimate that is only assumed to be accurate over a small region. Using the covariance matrix of the estimated transformation parameters as its guide, it “bootstraps” both the region over which the model is applied and choice of transformation models. It uses a robust version of standard ICP in each bootstrap iteration. In the context of retinal image registration, when combined with an initialization technique based on matching single landmarks or pairs of landmarks, it has shown nearly flawless performance in matching a large set of retinal image pairs. The Dual-Bootstrap ICP algorithm should be used in place of standard ICP when the combination of modeling and point transfer error of an initial transformation is comparable to the distance between different curves or surfaces in the data. Viewed another way, it substantially reduces the requirements on initial matching conditions in a registration or alignment problem so that only a “toe hold” on the alignment is required of an initial transformation.

The development of the algorithm raises additional challenges in registration, and these are the focus of our ongoing work. Most importantly, in the context of retinal image registration, the success of the algorithm, somewhat counter-intuitively, has thrown the research challenge back at feature extraction. The algorithm so successfully exploits whatever data are available that truly the only cause of failure is extremely poor quality image data leading to substantial missed or spurious features. Thus, robust, low-contrast feature extraction is our ongoing focus in retinal image registration.

8 Acknowledgements

The authors would like to thank the staff at the Center for Sight, especially Dr. Howard Tanenbaum and Dr. Anna Majerovics, for help in understanding retinal diseases and diagnostic techniques. We are thankful to Dr. Ali Can for discussions and valuable suggestions. Various portions of this research was supported by the National Science Foundation Experimental Partnerships grant EIA-0000417, the Center for Subsurface Sensing and Imaging Systems, under the Engineering Research Centers Program of the National Science Foundation (Award Number EEC-9986821), the National Institutes for Health grant RR14038, and by Rensselaer Polytechnic Institute.

References

- [1] R. Benjemaa and F. Schmitt. Fast global registration of 3d sampled surfaces using a multi-z-buffer technique. *Image and Vision Computing*, 17(2):113–123, 1999.
- [2] J. Bergen, P. Anandan, K. Hanna, and R. Hingorani. Hierarchical model-based motion estimation. In *Proceedings Second European Conference on Computer Vision*, pages 237–252, 1992.
- [3] P. Besl and N. McKay. A method for registration of 3-d shapes. *IEEE Transactions on Pattern Analysis and Machine Intelligence*, 14(2):239–256, 1992.
- [4] T. Binford and T. Levitt. Quasi-invariants: Theory and exploitation. In *Proceedings of the DARPA Image Understanding Workshop*, pages 819–829, 1993.
- [5] G. Blais and M. Levine. Registering multiview range data to create 3d computer objects. *IEEE Transactions on Pattern Analysis and Machine Intelligence*, 17(8):820–824, August 1995.
- [6] G. Borgefors. Distance transformations in digital images. *Computer Vision, Graphics, and Image Processing*, 34(3):344–371, June 1986.
- [7] K. Bubna and C. V. Stewart. Model selection techniques and merging rules for range data segmentation algorithms. *Computer Vision and Image Understanding*, 80:215–245, 2000.

- [8] A. Can, H. Shen, J. N. Turner, H. L. Tanenbaum, and B. Roysam. Rapid automated tracing and feature extraction from live high-resolution retinal fundus images using direct exploratory algorithms. *IEEE Trans. on Info. Tech. for Biomedicine*, 3(2):125–138, 1999.
- [9] A. Can, C. Stewart, and B. Roysam. Robust hierarchical algorithm for constructing a mosaic from images of the curved human retina. In *Proceedings IEEE Conference on Computer Vision and Pattern Recognition*, pages 286–292, 1999.
- [10] A. Can, C. Stewart, B. Roysam, and H. Tanenbaum. A feature-based algorithm for joint, linear estimation of high-order image-to-mosaic transformations: Mosaicing the curved human retina. *IEEE Transactions on Pattern Analysis and Machine Intelligence*, 24(3):412–419, 2002.
- [11] A. Can, C. Stewart, B. Roysam, and H. Tanenbaum. A feature-based, robust, hierarchical algorithm for registering pairs of images of the curved human retina. *IEEE Transactions on Pattern Analysis and Machine Intelligence*, 24(3):347–364, 2002.
- [12] G. Champlébois, S. Lavalée, R. Szeliski, and L. Brunie. From accurate range imaging sensor calibration to accurate model-based 3-d object localization. In *Proceedings IEEE Conference on Computer Vision and Pattern Recognition*, pages 83–89, 1992.
- [13] C. Chen, Y. Hung, and J. Cheng. RANSAC-based DARCES: A new approach to fast automatic registration of partially overlapping range images. *IEEE Transactions on Pattern Analysis and Machine Intelligence*, 21(11):1229–1234, November 1999.
- [14] Y. Chen and G. Medioni. Object modeling by registration of multiple range images. *Image and Vision Computing*, 10(3):145–155, 1992.
- [15] C. K. Chow, H. T. Tsui, T. Lee, and T. K. Lau. Medical image registration and model construction using genetic algorithms. In *Proc. of Int. Workshop on Medical Imaging and Augmented Reality*, pages 174–179, 2001.
- [16] C. Chua and R. Jarvis. 3d free-form surface registration and object recognition. *International Journal of Computer Vision*, 17(1):77–99, 1996.
- [17] H. Chui and A. Rangarajan. A new algorithm for non-rigid point matching. In *Proceedings IEEE Conference on Computer Vision and Pattern Recognition*, pages II:44–51, 2000.

- [18] T. Clark, W. Freeman, and M. Goldbaum. Digital overlay of fluorescein angiograms and fundus images for treatment of subretinal neovascularization. *Retina*, 12:118–26, 1992.
- [19] A. Collignon, D. Vandermeulen, P. Suetens, and G. Marchal. Registration of 3d multi-modality medical images using surfaces and point landmarks. *Pattern Recognition Letters*, 15(5):461–467, 1994.
- [20] M. Colthurst, R. Williams, P. Hiscott, and I. Grierson. Biomaterials used in the posterior segment of the eye. *Biomaterials*, 21(7):649–665, April 2000.
- [21] P.-E. Danielsson. Euclidean distance mapping. *Computer Graphics and Image Processing*, 14:227–248, 1982.
- [22] J. S. Duncan and N. Ayache. Medical image analysis: progress over two decades and the challenges ahead. *IEEE Transactions on Pattern Analysis and Machine Intelligence*, 22(1):85–105, 2000.
- [23] J. Feldmar and N. Ayache. Rigid, affine and locally affine registration of free-form surfaces. *International Journal of Computer Vision*, 18(2):99–119, 1996.
- [24] J. Feldmar, J. Declerck, G. Malandain, and N. Ayache. Extension of the ICP algorithm to nonrigid intensity-based registration of 3d volumes. *Computer Vision and Image Understanding*, 66(2):193–206, May 1997.
- [25] S. Fine. Observations following laser treatment for choroidal neovascularization. *Archives of Ophthalmology*, 106:1524–1525, 1988.
- [26] M. A. Fischler and R. C. Bolles. Random Sample Consensus: A paradigm for model fitting with applications to image analysis and automated cartography. *CACM*, 24:381–395, 1981.
- [27] K. Fritzsche, A. Can, H. Shen, C. Tsai, J. Turner, H. Tanenbaum, C. Stewart, and B. Roysam. Automated model based segmentation, tracing and analysis of retinal vasculature from digital fundus images. In J. S. Suri and S. Laxminarayan, editors, *State-of-The-Art Angiography, Applications and Plaque Imaging Using MR, CT, Ultrasound and X-rays*. Academic Press, 2002.

- [28] D. Geroski and H. Edelhauser. Transscleral drug delivery for posterior segment disease. *Advanced Drug Delivery Reviews*, 52(1):37–48, Oct 2001.
- [29] W. Grimson, T. Lozano-Perez, W. Wells, G. Ettinger, and S. White. An automatic registration method for frameless stereotaxy, image, guided surgery and enhanced reality visualization. In *Proceedings IEEE Conference on Computer Vision and Pattern Recognition*, pages 430–436, 1994.
- [30] A. Gueziec, X. Pennec, and N. Ayache. Medical image registration using geometric hashing. *IEEE Computational Science and Engineering*, 4(4):29–41, 1997.
- [31] F. R. Hampel, P. J. Rousseeuw, E. Ronchetti, and W. A. Stahel. *Robust Statistics: The Approach Based on Influence Functions*. John Wiley & Sons, 1986.
- [32] C. Harris and M. Stephens. A combined corner and edge detector. In *Proc. 4th Alvey Vision Conference*, pages 147–151, 1988.
- [33] R. Hartley and A. Zisserman. *Multiple View Geometry*. Cambridge University Press, 2000.
- [34] T. Hellstedt and I. Immonen. Disappearance and formation rates of microaneurysms in early diabetic retinopathy. *Br. J. Ophthalmology*, 6:135–139, 1999.
- [35] K. Higuchi, M. Hebert, and K. Ikeuchi. Building 3-d models from unregistered range images. *Graphical Models and Image Processing*, 57(4):315–333, 1995.
- [36] P. W. Holland and R. E. Welsch. Robust regression using iteratively reweighted least-squares. *Commun. Statist.-Theor. Meth.*, A6:813–827, 1977.
- [37] P. J. Huber. *Robust Statistics*. John Wiley & Sons, 1981.
- [38] A. Johnson and M. Hebert. Surface matching for object recognition in complex 3-dimensional scenes. *Image and Vision Computing*, 16(9-10):635–651, July 1998.
- [39] A. Johnson and S. Kang. Registration and integration of textured 3-d data. *Image and Vision Computing*, 17(2):135–147, 1999.
- [40] R. Kaiser, J. Berger, M. Maguire, A. Ho, N. Javornik, and C. N. P. T. S. Group. Laser burn intensity and the risk for choroidal neovascularization in the cnvpt fellow eye study. *Archives of Ophthalmology*, 119(6):826–832, Jun 2001.

- [41] C. Klaver, J. Assink, R. van Leeuwen, R. Wolfs, J. Vingerling, T. Stijnen, A. Hofman, and P. de Jong. Incidence and progression rates of age-related maculopathy: the rotterdam study. *Investigative Ophthalmology & Visual Science*, 42(10):2237–2241, Sep 2001.
- [42] E. Kohner, I. Sleightholm, S. Aldington, R. Turner, and D. Matthews. Microaneurysms in the development of diabetic retinopathy. *Diabetologia*, 42:1107–1112, 1999.
- [43] M. Levoy, K. Pulli, B. Curless, S. Rusinkiewicz, S. Anderson, J. Davis, J. Ginsberg, J. Shade, and D. Fulk. The Digital Michelangelo Project: 3d scanning of large statues. In *Proceedings of SIGGRAPH 2000*, pages 131–144, 2000.
- [44] Y. Liu and M. Rodrigues. Eliminating false matches in image registration through geometric histograms from reflected correspondence vectors. In *Proc. Int. Conf. on Intelligent Robots and Systems*, volume 4, pages 1997–2002, 2001.
- [45] J. Luck, C. Little, and W. Hoff. Registration of range data using a hybrid simulated annealing and iterative closest point algorithm. In *Proceedings IEEE International Conference on Robotics and Automation*, pages 3739–3744, April 2000.
- [46] T. Masuda and N. Yokoya. A robust method for registration and segmentation of multiple range images. *Computer Vision and Image Understanding*, 61(3):295–307, 1995.
- [47] G. K. Matsopoulos, N. A. Mouravliansky, K. K. Delibasis, and K. S. Nikita. Automatic retinal image registration scheme using global optimization techniques. *IEEE Transactions on Information Technology in Biomedicine*, 3(1):47–60, 1999.
- [48] D. Matthews, E. Kohner, S. Aldington, and I. Stratton. Relationship of microaneurysms count to progression of retinopathy over 6 years in non-insulin-dependent diabetes. *Diabetes*, 9:117A, 1995.
- [49] C.-H. Menq, H.-T. Yau, and G.-Y. Lai. Automated precision measurement of surface profile in CAD-directed inspection. *IEEE Transactions on Robotics and Automation*, 8(2):268–278, 1992.
- [50] J. V. Miller. *Regression-Base Surface Reconstruction: Coping with Noise, Outliers, and Discontinuities*. PhD thesis, Rensselaer Polytechnic Institute, 1997.

- [51] J. V. Miller and C. V. Stewart. MUSE: Robust surface fitting using unbiased scale estimates. In *Proceedings IEEE Conference on Computer Vision and Pattern Recognition*, pages 300–306, 1996.
- [52] R. Mittre and W. Mieler. *Retina*, volume 2, chapter 111. Drug Toxicity of the Posterior Segment. Mosby, 2001. 1779–1796.
- [53] J. Mundy and A. Zisserman, editors. *Geometric Invariance in Computer Vision*. MIT Press, 1992.
- [54] V. Murino, L. Ronchetti, U. Castellani, and A. Fusiello. Reconstruction of complex environments by robust pre-aligned ICP. In *Proc. Third Int. Conf. on 3-D Digital Imaging and Modeling*, pages 187–194, 2001.
- [55] V.-D. Nguyen, V. Nzomigni, and C. Stewart. Fast and robust registration of 3d surfaces using low curvature patches. In *Proc. 2nd Int. Conf. on 3D Digital Imaging and Modeling*, pages 201–208, 1999.
- [56] N. Ritter, R. Owens, J. Cooper, R. Eikelboom, and P. van Saarloos. Registration of stereo and temporal images of the retina. *IEEE Transactions on Medical Imaging*, 18(5):404–418, 1999.
- [57] P. J. Rousseeuw. Least median of squares regression. *Journal of the American Statistical Association*, 79:871–880, 1984.
- [58] P. J. Rousseeuw and C. Croux. Alternatives to the median absolute deviation. *Journal of the American Statistical Association*, 88:1273–1283, 1993.
- [59] P. J. Rousseeuw and A. M. Leroy. *Robust Regression and Outlier Detection*. John Wiley & Sons, 1987.
- [60] S. Rusinkiewicz and M. Levoy. Efficient variants of the ICP algorithm. In *Proc. Third Int. Conf. on 3-D Digital Imaging and Modeling*, pages 224–231, 2001.
- [61] S. Russell and G. Hageman. Optic disc, foveal, and extrafoveal damage due to surgical separation of the vitreous. *Archives of Ophthalmology*, 119(11):1653–1658, Nov 2001.

- [62] H. Sawhney, S. Hsu, and R. Kumar. Robust video mosaicing through topology inference and local to global alignment. In *Proceedings 5th European Conference on Computer Vision*, volume II, pages 103–119, 1998.
- [63] H. Sawhney and R. Kumar. True multi-image alignment and its application to mosaicing and lens distortion correction. *IEEE Transactions on Pattern Analysis and Machine Intelligence*, 21(3):235–243, 1999.
- [64] C. Schmid, R. Mohr, and C. Bauckhage. Comparing and evaluating interest points. In *Proceedings IEEE International Conference on Computer Vision*, pages 230–235, 1998.
- [65] G. Sharp, S. Lee, and D. Wehe. ICP registration using invariant features. *IEEE Transactions on Pattern Analysis and Machine Intelligence*, 24(1):90–102, 2002.
- [66] H. Shen, B. Roysam, C. Stewart, J. Turner, and H. Tanenbaum. Optimal scheduling of tracing computations for real-time vascular landmark extraction from retinal fundus images. *IEEE Transactions on Information Technology in Biomedicine*, 5(1):77–91, Mar 2001.
- [67] H. Shen, C. Stewart, B. Roysam, G. Lin, and H. Tanenbaum. Frame-rate spatial referencing based on invariant indexing and alignment with application to laser retinal surgery. In *Proceedings IEEE Conference on Computer Vision and Pattern Recognition*, volume 1, pages 79–86, 2001.
- [68] J. Shi and C. Tomasi. Good features to track. In *Proceedings IEEE Conference on Computer Vision and Pattern Recognition*, pages 593–600, 1994.
- [69] G. Soubrane, C. Coscas, G. amd Francais, and F. Koenig. Occult subretinal new vessels in age-related macular degeneration. *Ophthalmology*, 97:649–657, 1990.
- [70] C. V. Stewart. Robust parameter estimation in computer vision. *SIAM Reviews*, 41(3), September 1999.
- [71] A. Stoddart, S. Lemke, A. Hilton, and T. Renn. Estimating pose uncertainty for surface registration. *Image and Vision Computing*, 16(2):111–120, 1998.
- [72] R. Szeliski and S. Lavallee. Matching 3-d anatomical surfaces with non-rigid deformations using octree-splines. *International Journal of Computer Vision*, 18(2):171–186, 1996.

- [73] The Macular Photocoagulation Study Group. The use of fundus photographs and fluorescein angiograms in the identification and treatment of choroidal neovascularization in the macular photocoagulation study. *Ophthalmology*, 96:1526–1534, 1989.
- [74] J. Thirion. New feature points based on geometric invariants for 3d image registration. *International Journal of Computer Vision*, 18(2):121–137, 1996.
- [75] P. Torr. An assessment of information criteria for motion model selection. In *Proceedings IEEE Conference on Computer Vision and Pattern Recognition*, pages 47–52, 1997.
- [76] P. Torr and D. Murray. The development and comparison of robust methods for estimating the fundamental matrix. *International Journal of Computer Vision*, 24(3):271–300, 1997.
- [77] P. Torr and A. Zisserman. MLESAC: A new robust estimator with application to estimating image geometry. *Computer Vision and Image Understanding*, 78(1):138–156, April 2000.
- [78] Z. Zhang. Iterative point matching for registration of free-form curves and surfaces. *International Journal of Computer Vision*, 13(2):119–152, 1994.
- [79] Z. Zhang. Determining the epipolar geometry and its uncertainty: A review. *International Journal of Computer Vision*, 27(2):161–195, 1998.